Heliyon 10 (2024) e23396

Contents lists available at ScienceDirect

Heliyon

journal homepage: www.cell.com/heliyon

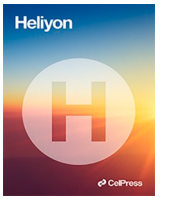

Two-dimensional $LiTi_2(PO_4)_3$ flakes for enhanced lithium ions battery anode

Yaxuan He [a], Zehao Zhang [a], Guolin Feng [b], Haibo Li [a,*]

[a] Ningxia Key Laboratory of Photovoltaic Materials, School of Materials and New Energy, Ningxia University, Yinchuan 750021, China
[b] School of Physics and Electronic Information Engineering, Ningxia Normal University, Guyuan 756000, China

ARTICLE INFO

Keywords:
$LiTi_2(PO_4)_3$
Lithium-ion batteries
Anode
NASICON-Type structure

ABSTRACT

In this work, the $LiTi_2(PO_4)_3$ (LTP) flakes have been prepared by employing a template method for lithium-ion batteries with high capacity. The 2D layered structure of LTP offers large aspect ratio and rich active sites, which not only create the large contact area between the electrolyte and electrode, but also promote the diffusion kinetics of Li^+. As a result, the Li^+ diffusion coefficient of lamellar LTP anode is 3.12×10^{-8} cm^2 s^{-1}, while it is only 5.01×10^{-10} cm^2 s^{-1} for granular LTP anode. Further, the lamellar LTP anode delivers a high initial discharge capacity of 986.8 $mAh{\cdot}g^{-1}$ at 0.1 A g^{-1}, and remains at 231.1 $mAh{\cdot}g^{-1}$ after 100 cycles, which is higher than that of the granular LTP anode (340.5 $mAh{\cdot}g^{-1}$ at 1st cycle, 169.3 $mAh{\cdot}g^{-1}$ at 100th cycles). Thus, the lamellar LTP should be recommended as a potential anode for high-performance LIBs due to the fast charge-discharge performance and superior cycling stability.

1. Introduction

Owing to the fast development of electric vehicles (EVs), it is very urgent to exploit high-power LIBs [1–5]. Currently, the graphite anode is the priority for LIBs towards the commercialization, which is cost-effective and stable as well as the abundant reserves [6–8]. Unfortunately, the inherent disadvantage associating with graphite anode is low Li^+ intercalation potential (0.1 V *vs.* Li^+/Li), which probably leads to the deposition of metal lithium, giving rise to safety issues and poor rate performance [9–11]. Alternatively, the promising insertion host materials, such as TiO_2, $Li_4Ti_5O_{12}$, $LiCrTiO_4$ and $LiTi_2(PO_4)_3$ (LTP) have been recommended as the potential anode instead of graphite [12–16]. Among these candidates, the polyanionic compound LTP with (NASICON)-type structure has demonstrated the high energy density and long life when served as the anode for LIBs. In terms of the superiorities of the LTP anode, they can be classified as below: (1) The 3D skeleton structure that formed by linking each TiO_6 octahedron and six PO_4 tetrahedrons sharing all the top O atom facilitates the Li^+ migration; (2) Each molar LTP stores 2 M Li^+; (3) The high strength of P–O covalent bond causes high thermal stability and ionic conductivity during the Li^+ insertion/de-insertion [17–21]. As a result, the theoretical specific capacity of LTP is 138 $mAh{\cdot}g^{-1}$ [22]. Despite the advances of LTP, it encounters inferior electronic conductivity, which undoubtedly brings high charge transfer resistance. To face this issue, many strategies have been proposed, such as morphological modification and composite engineering [23,24]. For example, *Zhou et al.* synthesized the $LiTi_2(PO_4)_3$/C nanoporous microplates (LTP/C MPs) using ethylenediamine as both the chelating agent and carbon source by a one-step solvothermal method. The LTP/C MPs consisted of interconnected LTP nano-particles which embedded in nano-thickness carbon layer (~10 nm) [25]. The novel porous plate structure

* Corresponding author.
E-mail address: lihaibo@nxu.edu.cn (H. Li).

https://doi.org/10.1016/j.heliyon.2023.e23396
Received 8 August 2023; Received in revised form 13 November 2023; Accepted 3 December 2023
Available online 7 December 2023

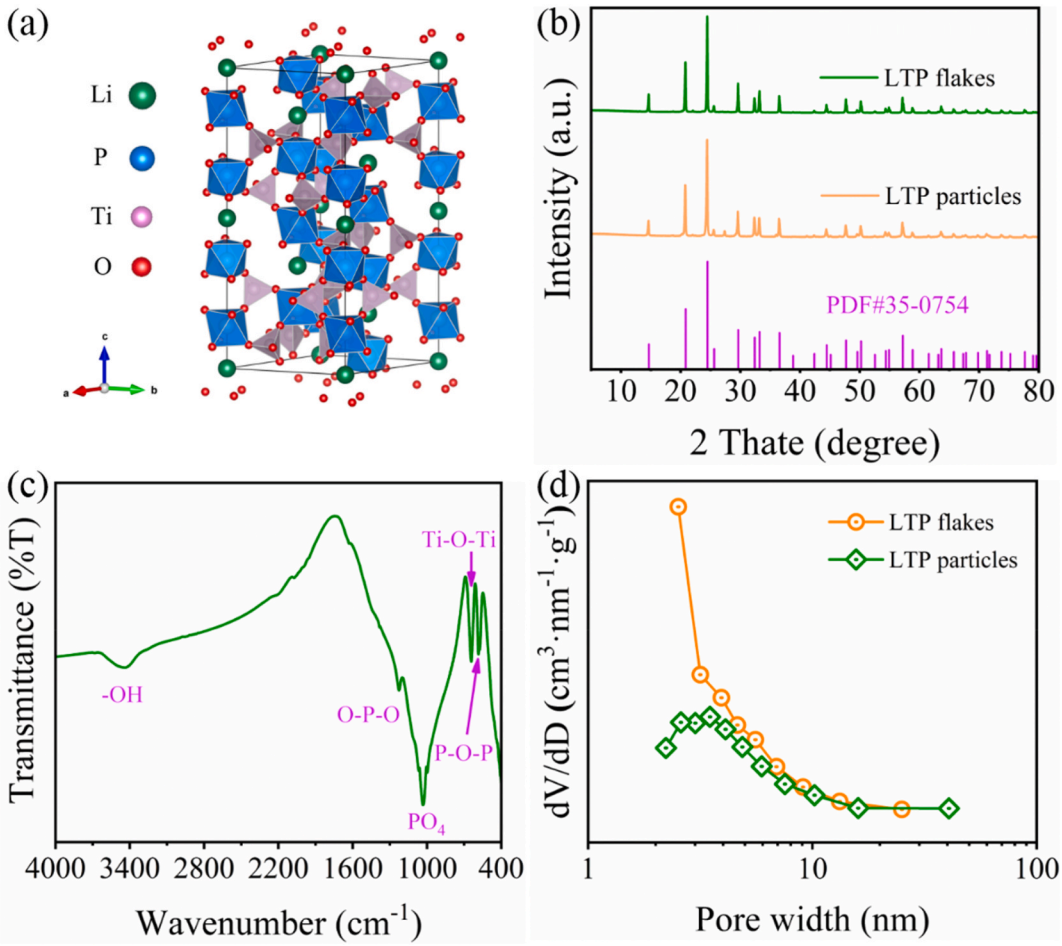

Fig. 1. (a) Crystal structure of LTP flakes, (b) XRD pattern of LTP flakes and LTP particles, (c) FTIR spectra of LTP flakes, (d) pore size distribution curves of LTP flakes and LTP particles.

enables to reduce the Li^+ diffusion distance and offer favorable conditions for electrolyte to penetrate the electrode completely. Meanwhile, the carbon layer generates the conductive network to improve the electronic conductivity of LTP microplates effectively. As a consequence, the as-prepared LTP/C MPs achieves a high capacity of 114 mAh·g^{-1} with a retention of about 94.2 % after 100 cycles at 0.2C. *Ye et al.* reported a facile sol-gel method to synthesize LTP anode, followed by introducing carbon coatings by carbonating β-cyclodextrin [26]. It realized that the uniform carbon coating can support a high Li^+ mobility and yield serviceable electronic conductivity. Thus, the LTP@carbon displayed high initial discharge specific capacity of 131.2 mAh·g^{-1} at 0.2C, and it remained at 90 % after 50 cycles.

Inspired the above investigations, we developed a templated sacrificial approach to prepare 2D LTP flakes enabling high Li^+ diffusion kinetics for enhanced LIBs. The morphology, structure and electrochemical performance of LTP were analyzed and discussed. As compared to LTP particles, the LTP flakes anode demonstrated improved specific capacity and prominent rate capability. Beyond that, the post characterization was performed to verify the reliability of the LTP anode.

2. Experimental section

The 2D TiO_2 nanoflakes as the template was prepared according to our previous work [27]. Firstly, 16 mg Li_2CO_3, 142.16 mg $(NH_4)H_2PO_4$ and 65 mg 2D TiO_2 nanoflakes were ground evenly in a mortar for 5 min to obtain homogenous mixture. Then, an appropriate amount of deionized water (DI) was added to the mortar, and the rheological mixture was formed after grinding. Afterwards, the mixture was dried at 100 °C for 8 h. Finally, the as-prepared precursor was ground in a mortar and annealed in a muffle furnace at 800 °C for 6 h, resulting in the synthesis of LTP flakes. The LTP particles were synthesized according to the same method while the commercial TiO_2 powders were utilized instead of 2D TiO_2 nanoflakes. The overall reaction involved in this process is written below [28]:

$$0.5Li_2CO_3 + 2TiO_2 + 3(NH_4)H_2PO_4 \rightarrow LiTi_2(PO_4)_3 + 3NH_3 + 0.5CO_2 + 4.5H_2O \quad (1)$$

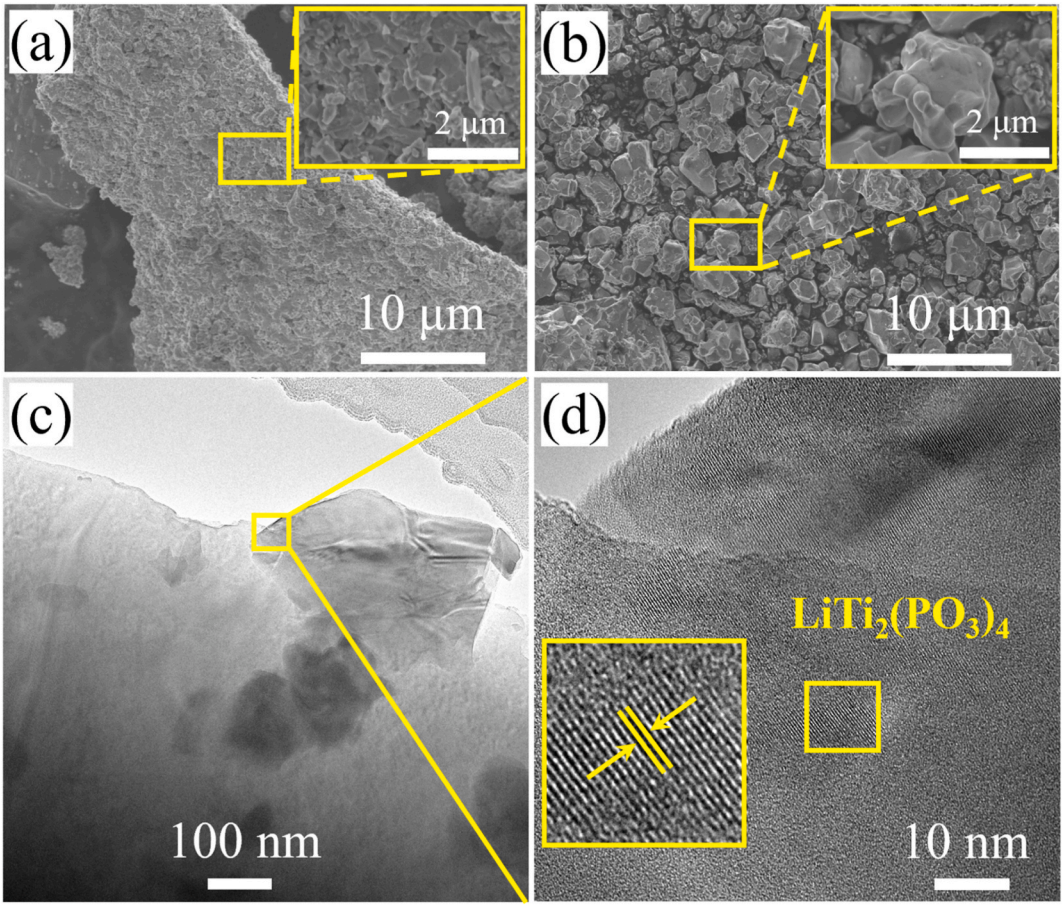

Fig. 2. SEM images of (a) LTP flakes and (b) LTP particles, (c) TEM and (d) HRTEM images of LTP flakes.

The preparation of the anode and the assembly of the battery have been described somewhere [29,30]. Specifically, the copper foam with a diameter of 1.2 cm was employed as the current collector. Then, the as-prepared active material, acetylene black and binder (PVDF) were mixed together according to the mass ratio of 8: 1: 1. After that, they were ground at least 10 min to achieve the even mixing. Meanwhile, few drops of NMP were added into the mixture to make it moisture. Further, the slurry was uniformly coated on the copper foam and then dry at 80 °C for 12 h in air. Finally, the battery was assembled in a glove box filling with argon. The galvanostatic charge-discharge (GCD) performance of the lamellar LTP anode and granular LTP anode was obtained on a battery test system (CT2001A, LANHE, China) at ambient temperature. The electrochemical workstation (PARSTAT 3000 A-DX, Princeton Applied Research, USA) was used to explore the electrochemical impedance spectrum (EIS) and cyclic voltammetry (CV) profiles of the lamellar LTP anode and granular LTP anode.

3. Results and discussion

Fig. 1a draws the crystal structure of LTP flakes. It is found that the 3D skeleton structure is constituted by connecting TiO_6 octahedron and PO_4 tetrahedron. Such rhombohedral NASICON-type structure effectively facilitates the Li^+ transport [31,32]. The crystalline phase of LTP flakes and LTP particles are explored by the X-ray diffraction (XRD; Smart Lab, Japan) and the corresponding XRD patterns are shown in Fig. 1b. All relevant characteristic diffraction peaks of the LTP flakes and LTP particles are associating with the rhombohedral NASICON-type LTP very well (space group *R*3*c*, PDF#35–0754) [33]. Moreover, the peaks are sharp and strong, suggesting the high purity and crystallinity. Specifically, the main characteristic diffraction peaks distribute at 14.7°, 20.8°, 24.5°, 25.6°, 29.6°, 32.4°, 33.2°, 36.5° and 57.2°, which corresponds to the (012), (104), (113), (202), (024), (211), (116), (300) and (410) crystal planes of LTP flakes and LTP particles, respectively. Fig. 1c shows the Fourier transform infrared spectrum (FTIR; spectrum Two03040404, USA) of LTP flakes. Essentially, the band emerging at 578.1 cm^{-1} and 643.8 cm^{-1} are relating to the P–O–P bond in the PO_4 tetrahedron and the Ti–O–Ti bond in the TiO_6 octahedron, respectively. The sharp absorption peak at 1040 cm^{-1} belongs to the stretching vibration of PO_4 functional group in the LTP flakes. Further, the absorption peak near 1226 cm^{-1} corresponds to the stretching vibration of the O–P–O non-bridge oxygen bonds. Besides, peaks presenting at 3437.7 cm^{-1} and 1633 cm^{-1} are separately attributed to the bending vibration and symmetrical stretching vibration modes of –OH due to the water absorbed from the KBr and

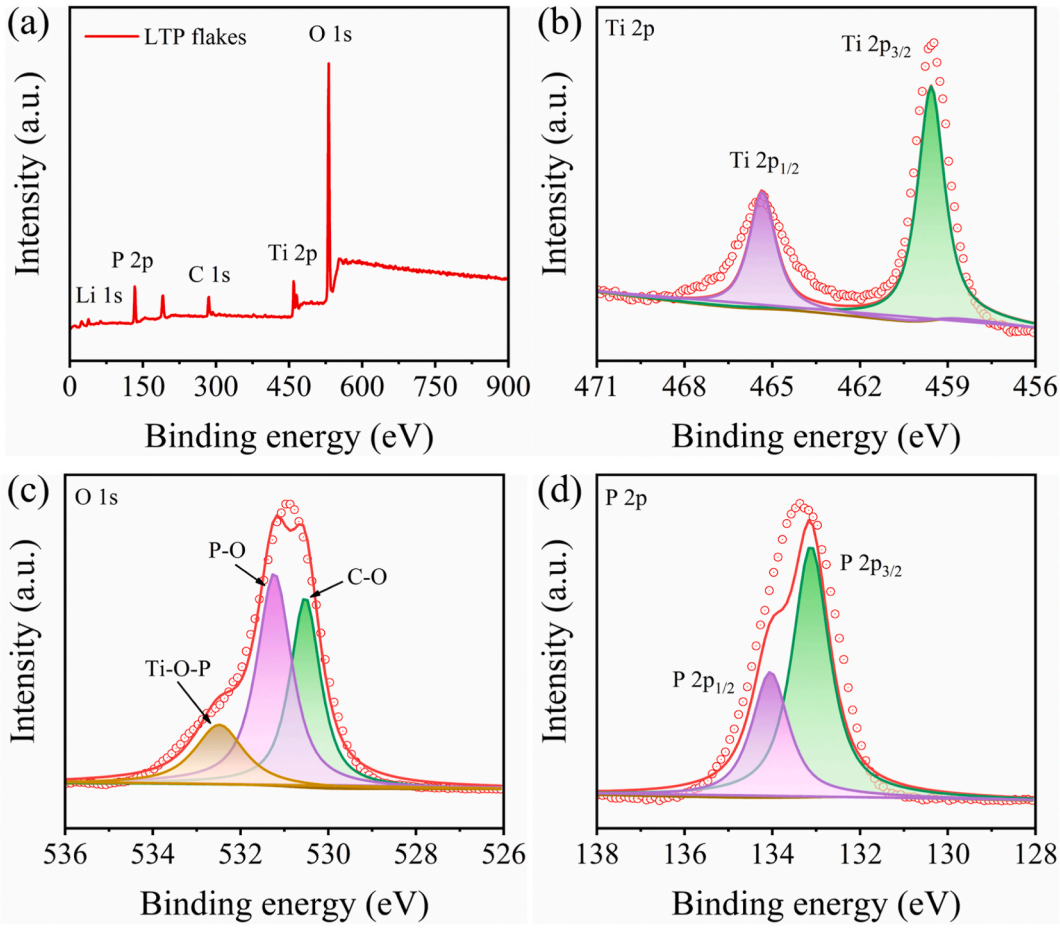

Fig. 3. (a) Full XPS spectrum, (b) Ti 2p, (c) O 1s and (d) P 2p spectrum of LTP flakes.

phosphate matrix. The Brunauer-Emmett-Teller (BET) and Barrett-Joyner-Halenda (BJH) methods were employed to detect the dates of specific surface area and the pore size distributions by a surface area analyzer (JW-BK200C, China). Fig. 1d shows the pore size distribution curve of LTP flakes and LTP particles. The dominant peaks concentrate at 3.26 nm and 2.89 nm, respectively, corresponding to LTP flakes and LTP particles.

Fig. 2a and b shows the scanning electron microscopy (SEM; Hitachi SU5000, Japan) images of LTP flakes and LTP particles, respectively. In Fig. 2a, the tightly connected LTP particles constitute LTP flakes. This novel structure helps to enlarge the contact area between the electrolyte and the LTP, which enable the rapid electrons transfer and fast Li^+ diffusion. In Fig. 2b, the rock-like LTP particles randomly stack together, which is not conducive to Li^+ migration. Moreover, the high-resolution transmission electron microscopy (HRTEM; FEI Talos200s, USA) images of LTP flakes are illuminated in Fig. 2c and d. Obviously, the layered structure is confirmed, and a lattice fringe with a lattice spacing of 0.368 nm can be measured, which corresponds to the (113) crystal plane of LTP.

The chemical valence state of elements of LTP flakes was studied by X-ray photoelectron spectrum (XPS, Thermo ESCALAB 250Xi). Fig. 3a displays the XPS full survey spectrum of LTP flakes, which exhibits the characteristic peaks of O 1s, Ti 2p, C 1s, P 2p and Li 1s. The high-resolution Ti 2p XPS spectrum was shown in Fig. 3b, the existence state of Ti in the sample was further confirmed. Two characteristic peaks staying at 459.6 eV and 465.4 eV are corresponding to the spin-orbit splitting photoelectrons of Ti $2p_{3/2}$ and Ti $2p_{1/2}$ in the chemical state of Ti^{4+}, respectively [34]. Fig. 3c shows the O 1s spectrum. Three dominant peaks locating at 530.5 eV, 531.2 eV and 532.5 eV separately represent the C–O, P–O and Ti–O–P bonds. In Fig. 3d, it relates to the P 2p spectrum, in which the binding energies of 132.9 eV and 134.2 eV is associating with the P $2p_{3/2}$ and P $2p_{1/2}$, respectively.

The CV measurement of lamellar LTP anode was carried out at 0.1 mV s^{-1} within the potential window ranging from 1.5 V to 3.0 V under room temperature. Fig. 4a draws the CV curves of the first four cycles. It can be observed that a pair of redox peaks appearing at 2.41 V/2.57 V relate to the valence state of Ti varying from +4 to +3 undergoing the insertion/de-insertion of Li^+. Moreover, the low voltage difference 0.16 V between the oxidation peak and the reduction peak indicates the high reversibility of lamellar LTP anode. Basically, the reduction peak emerging at 1.6 V may be attributed to the formation of solid electrolyte interface film as well as the decomposition of electrolyte. The cycling performance of lamellar LTP anode and granular LTP anode were evaluated at 0.1 A g^{-1} in Fig. 4b. Appreciably, the initial discharge specific capacity of lamellar LTP were as high as 986.8 mAh·g^{-1}, while the corresponding

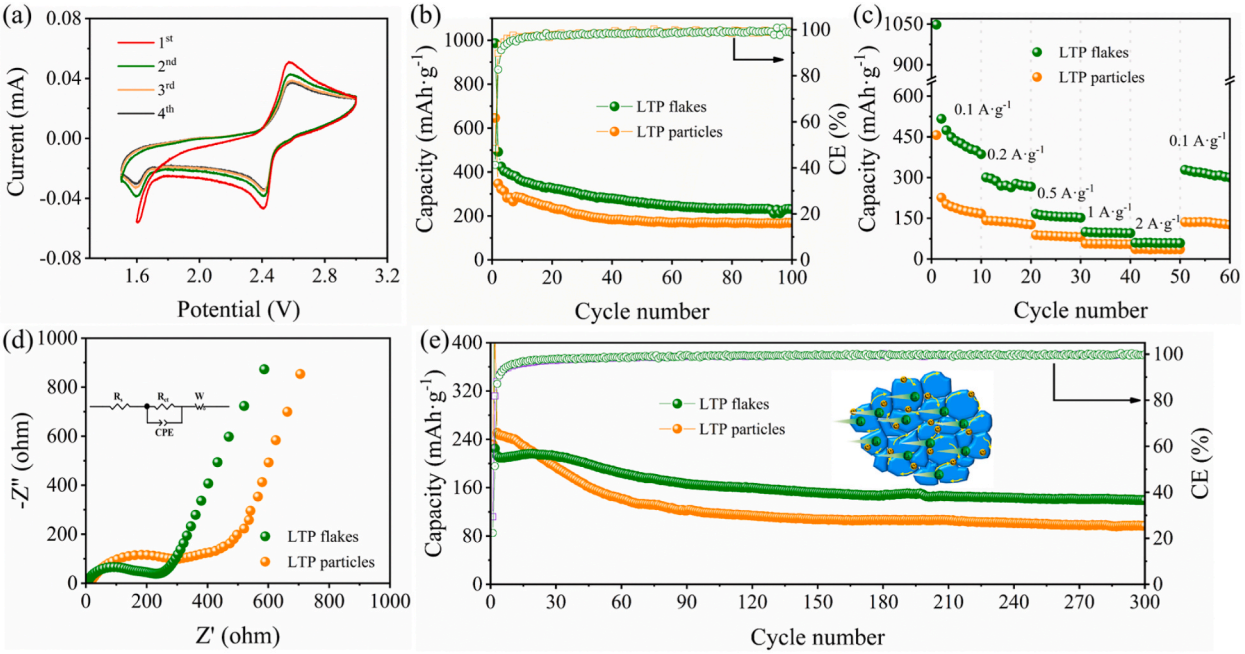

Fig. 4. (a) CV curve of lamellar LTP anode, the (b) cycling performance, (c) rate performance, (d) EIS spectra and (e) long-term cycling performance of lamellar LTP anode and granular LTP anode.

Table 1
Comparison of the LIB performance of NASICON type-based anodes.

Sample	Capacity/(mAh·g^{-1})	Ref.
Rhombohedral $LiTi_2(PO_4)_3$	122 at 15 mA g^{-1}	[17]
LTP/C	144 at 28 mA g^{-1} after 100 cycles	[19]
$LiTi_2(PO_4)_3$@carbon	133.1 at 27.6 mA g^{-1}	[26]
$LiTi_2(PO_4)_3$	360 at 20 mA g^{-1}	[28]
C–$LiTi_2(PO_4)_3$	94.6 at 0.5 mA cm^{-1} after 50 cycles	[35]
$NaTi_2(PO_4)_3$/C	390.7 at 100 mA g^{-1} after 100 cycles	[36]
rGO/NTP	400.9 at 100 mA g^{-1} after 200 cycles	[37]
LTP/C	143.4 at 14.4 mA g^{-1}	[38]
$LiTi_2(PO_4)_3$/C	113.4 at 138 mA g^{-1} after 100 cycles	[39]
This work	231.1 at 100 mA g^{-1} after 100 cycles	

value is 646.3 mAh·g^{-1} in terms of granular LTP. After 100 cycles, the lamellar LTP anode remains at 231.1 mAh·g^{-1}, which is much higher than that of granular LTP (169.3 mAh·g^{-1}). Further, the coulombic efficiency (CE) of lamellar LTP anode and granular LTP anode reach to 98.6 % and 98.7 % after 100 cycles, respectively. Table 1 summarizes the specific capacities of various NASICON type-based electrodes for comparison. Rate performance of lamellar LTP and granular LTP were investigated under various rates of 0.1 A g^{-1}, 0.2 A g^{-1}, 0.5 A g^{-1}, 1 A g^{-1}, 2 A g^{-1} and 0.1 A g^{-1}. As illuminated in Fig. 4c, the discharge specific capacities of lamellar LTP are higher than that of granular LTP at any current density. Upon the rate increasing, the discharge specific capacities gradually decrease for both anodes, which is presumably ascribed to the electrochemical polarization under large current. Further, when the current density varies from 2 A g^{-1} to 0.1 A g^{-1}, the discharge specific capacity of lamellar LTP maintains at 300 mAh·g^{-1}, indicating the superior rate capability. Fig. 4d shows the EIS spectra and corresponding Nyquist plots of lamellar LTP and granular LTP, the inset is the fitted equivalent circuit. The intercept at Z′ axis at high frequency is relating to the ohmic resistance (R_s) of electrolyte and electrode [40], while the semicircle at middle frequency represents the charge transfer resistance (R_{ct}) [41]. The R_{ct} of lamellar LTP and granular LTP is 537.7 Ω, and 810.3 Ω, respectively. The low R_{ct} of lamellar LTP may be ascribed to the layered structure which improves the electrochemical kinetics. In order to further study the Li^+ transport characteristics of lamellar LTP anode and granular LTP anode, the diffusion coefficient of lithium ions (D_{Li}^+) was calculated by the following formula [42,43]:

$$D_{Li^+} = R^2T^2/2A^2n^4F^4C^2\sigma^2 \quad (2)$$

where R is the gas constant, T is the tested absolute temperature of test condition, A is the surface area of the working electrode, n is the number of electrons transfer in the redox reaction, F is Faraday constant, C is the Li^+ concentration in the solid phase of the electrode, and the σ is the slope of linear fitting of the plot of Z_w against $\omega^{-1/2}$. As a result, the lamellar LTP anode demonstrated

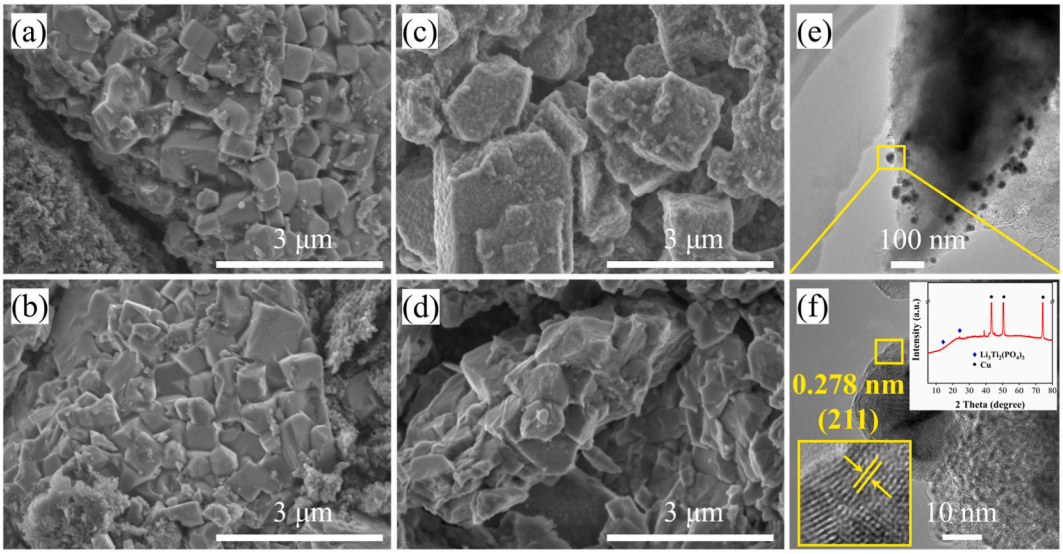

Fig. 5. SEM images of lamellar LTP from top and cross-sectional view before (a) and (b) and after (c) and (d) 100 cycling, (e) and (f) the HRTEM images of lamellar LTP anode after 100 cycling, the inset in (f) is the corresponding XRD pattern.

relatively higher $D_{Li}{}^{+}$ values than granular LTP anode, which is 3.12×10^{-8} cm^2 s^{-1} and 5.01×10^{-10} cm^2 s^{-1}, respectively. Fig. 4e shows the cycling capacity and CE of lamellar LTP anode and granular LTP anode at 1 A g^{-1}. Even at high current density, the lamellar LTP anode also demonstrates high initial discharge specific capacity of 592.5 mAh·g^{-1}. After 300 cycles, the discharge specific capacity of the lamellar LTP anode can reach 137.2 mAh·g^{-1} after 300 cycles. By contrast, the initial discharge specific capacity of the granular LTP anode was 423.3 mAh·g^{-1} and the discharge specific capacity remained 97.2 mAh·g^{-1} after 300 cycles. Thus, the LTP with layered structure achieved wonderful rate performance and cycling stability. As a comparison, the previous work published by Deng et al. reported the discharge specific capacity of graphite anode is only about 50 mAh·g^{-1} after 650 cycles at a current density of 3C [44].

By studying the morphological and structural evolution of lamellar LTP anode upon the cycling, the Li^+ storage behavior was discussed. Fig. 5a and b are the SEM images of the lamellar LTP anode from the top view and cross section before cycling, respectively. The micro-sized LTP firmly connected together forming the lamellar structure. In Fig. 5c and d which exhibit the SEM image of corresponding lamellar LTP anode after 100 cycles at 0.1 A g^{-1}, the structural deterioration is rarely examined while the surface of LTP is covered by some small particles. It may be considered as $Li_3Ti_2(PO_4)_3$ that from the insertion of Li^+. Fig. 5e and f illuminate the HRTEM images of lamellar LTP anode after 100 cycles. The lattice fringes with lattice spacing of 0.278 nm can be marked, which correspond to the (211) crystal plane of $Li_3Ti_2(PO_4)_3$. Moreover, the corresponding XRD pattern is given in the insert of Fig. 5f. The diffraction peaks at 14.4° and 24.1° relating to the (012) and (113) crystal planes of $Li_3Ti_2(PO_4)_3$ are firmly determined, respectively.

4. Conclusions

In summary, the LTP flakes was successfully synthesized by template method for the enhanced anode with high Li^+ storage performance. The XRD analysis demonstrated that the as-prepared LTP flakes with highly crystallinity revealed the NASICON-structure. Moreover, it was proved the mesoporous texture, which is effective to exposure as much as electroactive sites and promote the diffusion kinetics of Li^+. For another, the tight connection of LTP particles can effectively shorten the diffusion path of Li^+. When LTP flakes is used as the anode of LIBs, it exhibited a high initial discharge capacity of 986.8 mAh·g^{-1} at a current density of 0.1 A g^{-1}, and remained at 231.1 mAh·g^{-1} after 100 cycles. It is noteworthy that the discharge specific capacity of the lamellar LTP anode can reach 137.2 mAh·g^{-1} after 300 cycles at a high current density of 1 A g^{-1}. Therefore, the LTP flakes is considered a prospective anode to be used in LIBs due to its superior fast charge and discharge performance and cycling stability.

Data availability statement

Data associated with this study has not been deposited into any publicly available repository. Data will be made available on request.

Additional information

No additional information is available for this paper.

CRediT authorship contribution statement

Yaxuan He: Writing – original draft, Investigation, Data curation. **Zehao Zhang:** Investigation, Data curation. **Guolin Feng:** Supervision, Investigation. **Haibo Li:** Writing – review & editing, Investigation, Funding acquisition, Conceptualization.

Declaration of competing interest

The authors declare that they have no known competing financial interests or personal relationships that could have appeared to influence the work reported in this paper.

Acknowledgements

This work was supported by the project of Ningxia Key R&D Plan (2021BEE03006) and Natural Science Foundation of Ningxia (No. 2021AAC05014).

References

[1] Q. Wei, Y.Y. Wu, S.J. Li, R. Chen, J.H. Ding, C.Y. Zhang, Spent lithium ion battery (LIB) recycle from electric vehicles: a mini-review, Sci. Total Environ. 866 (2023) 161380–161390.
[2] T.T. Luo, L. Wang, L. Dai, J.Y. Luo, S. Liu, A solid-state lithium metal battery with extended cycling and rate performance using a low-melting alloy interface, Inorg. Chem. Front. 10 (3) (2023) 1011–1017.
[3] S. Liu, X.Y. Zhang, R.S. Li, L.B. Gao, J.Y. Luo, Dendrite-free Li metal anode by lowering deposition interface energy with $Cu_{99}Zn$ alloy coating, Energy Storage Mater. 14 (2018) 143–148.
[4] Z.P. Cui, M. Sun, H.Q. Liu, S.J. Li, Q.Y. Zhang, C.P. Yang, G.J. Liu, J.Y. Zhong, Y.Q. Wang, Double-shell SnO_2@Fe_2O_3 hollow spheres as a high-performance anode material for lithium-ion batteries, CrystEngComm 22 (7) (2020) 1197–1208.
[5] T. Li, S.W. Gao, K. Li, G.J. Liu, X.L. Sheng, D.W. Shang, L.M. Wu, S.J. Chen, Y.Q. Wang, S.H. Wu, Tailoring the phase evolution of molybdenum-based nanocrystals in carbon nanofibers for enhanced performance of lithium-ion batteries, J. Alloys Compd. 934 (2023) 168042–168055.
[6] X.G. Liu, W. B Kang, X. Li, Z. Zeng, Y.J. Li, Q. Wang, C.H. Zhang, Solid-state mechanochemistry advancing two dimensional materials for lithium-ion storage applications: a mini review, Nano Materials Science 5 (2) (2023) 210–227.
[7] K.Q. Geng, M.Q. Yang, J.X. Meng, L.F. Zhou, Y.Q. Wang, D. Sydorov, Q. Zhang, S.W. Zhong, Q.X. Ma, Engineering layered/spinel heterostructure via molybdenum doping towards highly stable Li-rich cathodes, Tungsten 4 (2022) 323–335.
[8] A. Khan, B. Nilam, C. Rukhsar, G. Sayali, B. Mandlekar, A. Kadam, A review article based on composite graphene @tungsten oxide thin films for various applications, Tungsten 5 (2023) 391–418.
[9] X.L. Sheng, T. Li, M. Sun, G.J. Liu, Q.Y. Zhang, Z.B. Ling, S.W. Gao, F.Y. Diao, J.Z. Zhang, F. Rosei, Y.Q. Wang, Flexible electrospun iron compounds/carbon fibers: phase transformation and electrochemical properties, Electrochim. Acta 407 (2022) 139892–139905.
[10] S.H. Park, D. Jun, G.H. Lee, S.G. Lee, J.E. Jung, K.Y. Bae, S. Son, Y.J. Lee, Designing 3D anode based on pore-size-dependent Li deposition behavior for reversible Li-free all-solid-state batteries, Adv. Sci. 9 (28) (2022) 2203130–2203139.
[11] D.Y. Rhee, J. Kim, J. Moon, M.S. Park, Off-stoichiometric TiO_2-x-decorated graphite anode for high-power lithium-ion batteries, J. Alloys Compd. 843 (2020) 156042–156050.
[12] Y.J. Liu, R.Y. Fang, D. Miltin, NASICON solid electrolyte coated by indium film for all-solid-state Li-metal batteries, Tungsten 4 (2022) 316–322.
[13] S.I. Choi, E.J. Jung, M. Park, H.S. Shin, S. Huh, Y.S. Won, Phase-dependent performance of lotus-root shaped TiO_2 anode for lithium-ion batteries (LIBs), Appl. Surf. Sci. 508 (2020) 145237–145242.
[14] T. Yuan, Z.P. Tan, C.R. Ma, J.H. Yang, Z.F. Ma, S.Y. Zheng, Challenges of spinel $Li_4Ti_5O_{12}$ for lithium-ion battery industrial applications, Adv. Energy Mater. 7 (12) (2017) 1601625–1601650.
[15] Y.Q. Pi, W.Y. Sun, M.Y. Yan, F. Wang, D. Yu, Q.Y. An, Achieving high-performance energy storage device of $Li_3V_2(PO_4)_3$//$LiCrTiO_4$ Li-ion full cell, J. Power Sources 518 (2022) 230770–230778.
[16] Y.T. Wang, F.F. Zhang, J.A. Chen, X.M. Zhang, J.W. Wen, C.X. Wang, G.Y. Huang, Carbon-coated $LiTi_2(PO_4)_3$ composites synthesized through tannic acid with high-rate performance for aqueous lithium-ion batteries, J. Alloys Compd. 939 (2023) 168704–168722.
[17] Y. Kee, N. Dimov, K. Minami, S. Okada, Orthorhombic lithium titanium Phosphate as an anode material for Li-ion rechargeable battery, Electrochim. Acta 174 (2015) 516–520.
[18] B. Lang, B. Ziebarth, C. Elsaesser, Lithium-ion conduction in $LiTi_2(PO_4)_3$ and related compounds based on the NASICON structure: a first-principles study, Chem. Mater. 27 (2015) 5040–5048.
[19] H. El-Shinawi, J. Janek, Low-temperature synthesis of macroporous $LiTi_2(PO_4)_3$/C with superior lithium storage properties, RSC Adv. 5 (19) (2015) 14887–14891.
[20] A. Aatiq, M. Menetrier, L. Croguennec, E. Suard, C. Delmas, On the structure of $Li_3Ti_2(PO_4)_3$, J. Mater. Chem. 12 (10) (2002) 2971–2978.
[21] X. Hou, X.K. Ju, W.G. Zhao, J. Wang, X. He, L.L. Du, B. Yan, J.K. Li, E. Paillard, J.Y. Sun, H. Lin, M. Winter, J. Li, TiO_2@$LiTi_2(PO_4)_3$ enabling fast and stable lithium storage for high voltage aqueous lithium-ion batteries, J. Power Sources 484 (2021) 229255–229262.
[22] W.J. Deng, X.S. Wang, C.Y. Liu, C. Li, M.Q. Xue, R. Li, F. Pan, Touching the theoretical capacity: synthesizing cubic $LiTi_2(PO_4)_3$/C nanocomposites for high-performance lithium-ion battery, Nanoscale 10 (14) (2018) 6282–6287.
[23] Y.N. Zhou, M.Z. Xue, Z.W. Fu, Nanostructured thin film electrodes for lithium storage and all-solid-state thin-film lithium batteries, J. Power Sources 23 (2013) 310–332.
[24] L.L. Li, Y.H. Wen, H. Zhang, H. Ming, J. Pang, P.C. Zhao, G.P. Cao, A core@shell structured $LiTi_2(PO_4)_3$/C anode for aqueous lithium-ion batteries, Chemelectrochem 6 (6) (2019) 1908–1914.
[25] Z.F. Huang, L. Liu, Q. Zhou, J.L. Tan, Z.C. Yan, D.D. Xia, H.B. Shu, X.K. Yang, X.Y. Wang, Carbon-coated lithium titanium phosphate nanoporous microplates with superior electrochemical performance, J. Power Sources 294 (2015) 650–657.
[26] J.M. Ye, C.M. Li, Synthesis of $LiTi_2(PO_4)_3$@carbon anode material with superior performance using β-cyclodextrin as carbon sources, Ionics 26 (2) (2020) 2845–2853.
[27] Y.X. He, H.B. Li, Templated synthesis of 2D TiO_2 nanoflakes for durable lithium-ion batteries, New J. Chem. 4 (34) (2022) 16260–16264.
[28] G.X. Wang, D.H. Bradhurst, S.X. Dou, H.K. Liu, $LiTi_2(PO_4)_3$ with NASICON-type structure as lithium-storage materials, J. Power Sources 124 (2003) 231–236.
[29] Z.H. Zhang, H.B. Li, Sequential-template synthesis of hollowed carbon polyhedron@SiC@Si for lithium-ion battery with high capacity and electrochemical stability, Appl. Surf. Sci. 514 (2020) 145920–145928.
[30] Z.H. Zhang, Q.Z. Huang, W. Ma, H.B. Li, Interfacial engineering of polyhedral carbon@hollowed carbon@SiO_2 nanobox with tunable structure for enhanced lithium-ion battery, Appl. Surf. Sci. 538 (2021) 148039–148047.

[31] T. Xu, M.S. Zhao, Z. Su, W.Y. Duan, Y.Z. Shi, Z. Li, V.G. Pol, X.P. Song, Nanostructured $LiTi_2(PO_4)_3$ anode with superior lithium and sodium storage capability aqueous electrolytes, J. Power Sources 481 (2021) 229110–229121.
[32] J.Y. Pang, Q. Kuang, Y.M. Zhao, W. Han, Q.H. Fan, A comparative study of $LiTi_2(P_{8/9}V_{1/9}O_4)_3$ and $L_iTi_2(PO_4)_3$: synthesis, structure and electrochemical properties, Electrochim. Acta 260 (2018) 384–390.
[33] Z. Jiang, Y.H. Li, C. Han, Z.X. He, W. Meng, L. Dai, L. Wang, K doping on Li site enables $LiTi_2(PO_4)_3$/C excellent lithium storage performance, Solid State Ionics 34 (2019) 115036–115040.
[34] W.W. Sun, J.H. Liu, X.Q. Liu, X.J. Fan, K.A. Zhou, X.F. Wei, Bimolecular-induced hierarchical nanoporous $LiTi_2(PO_4)_3$/C with superior high-rate and cycling performance, Chem. Commun. 53 (62) (2017) 8703–8706.
[35] A. Vanchiappan, L.W. Chui, H. Steffen, B. Nicolas, M. Srinivasan, carbon-coated $LiTi_2(PO_4)_3$: an ideal insertion host for lithium-ion and sodium-ion batteries, Chem. Asian J. 9 (3) (2014) 878–882.
[36] Q. Yang, Z.Y. Li, H.L. Tian, Z. Su, Synthesis and characterization of NASICON-structured $NaTi_2(PO_4)_3$/C as an anode material for hybrid Li/Na-ion batteries, Ceram. Int. 45 (5) (2019) 6291–6295.
[37] Y.X. He, H.B. Li, Achieving high Li^+ diffusion in reduced graphene oxide/$NaTi_2(PO_4)_3$ heterostructures for enhanced lithium ions storage, J. Mater. Sci. 58 (2023) 455–4541.
[38] JiX. Sun, Y.R. Sun, L.G. Gai, H.H. Jiang, Y. Tian, Carbon-coated mesoporous $LiTi_2(PO_4)_3$ nanocrystals with superior performance for lithium-ion batteries, Electrochim. Acta 200 (2016) 66–74.
[39] W. Zhu, F.G. Niu, Y.P. Yang, Z.L. Wang, J. Yao, Z.G. Wang, Study of synthesis mechanism and electrochemical performance of $LiTi_2(PO_4)_3$, Asian J. Chem. 10 (26) (2014) 2916–2920.
[40] B.W. Yang, D.F. Wang, S.Q. Chen, X. Sun, B.K. Yu, Electrochemical impedance preprocessing with distribution of relaxation time transform, J. Power Sources 571 (2023) 233062–233075.
[41] D. Perry, M. Mamlouk, Probing mass transport processes in Li-ion batteries using electrochemical impedance spectroscopy, J. Power Sources 514 (2021) 230577–230589.
[42] H. Zhao, J.X. Chen, W.W. Wei, S.M. Ke, X.R. Zeng, D.C. Chen, P. Lin, The preparation of porous graphite and its application in lithium-ion batteries as anode material, Global Chall 4 (3) (2020) 1900073–1900080.
[43] M. Sun, X.L. Sheng, S.J. Li, Z.P. Cui, T. Li, Q.Y. Zhang, F. Xie, Y.Q. Wang, Construction of porous $CoTiO_3$ microrods with enhanced performance as lithium-ion battery anode, J. Alloys Compd. 926 (2022) 16618–166809.
[44] T.S. Deng, X.P. Zhou, The preparation of porous graphite and its application in lithium-ion batteries as anode material, J. Solid State Electrochem. 20 (2016) 2613–2618.